



Published in final edited form as:

J Pharm Sci. 2020 August ; 109(8): 2405–2412. doi:10.1016/j.xphs.2020.05.002.

Quantitative Differentiation of Protein Aggregates From Other Subvisible Particles in Viscous Mixtures Through Holographic Characterization

Annemarie Winters^a, Fook Chiong Cheong^a, Mary Ann Odete^a, Juliana Lumer^a, David B. Ruffner^a, Kimberly I. Mishra^{a,b}, David G. Grier^b, Laura A. Philips^{a,*}

^aSpheryx, Inc., 330 E. 38th St., New York, New York 10016

^bDepartment of Physics and Center for Soft Matter Research, New York University, New York, New York 10003

Abstract

We demonstrate the use of holographic video microscopy to detect individual subvisible particles dispersed in biopharmaceutical formulations and to differentiate them based on material characteristics measured from their holograms. The result of holographic analysis is a precise and accurate measurement of the concentrations and size distributions of multiple classes of subvisible contaminants dispersed in the same product simultaneously. We demonstrate this analytical technique through measurements on model systems consisting of human IgG aggregates in the presence of common contaminants such as silicone oil emulsion droplets and fatty acids. Holographic video microscopy also clearly identifies metal particles and air bubbles. Being able to differentiate and characterize the individual components of such heterogeneous dispersions provides a basis for tracking other factors that influence the stability of protein formulations including handling and degradation of surfactant and other excipients.

Keywords

Protein aggregates; Particle analysis; Particle characterization; Contaminants; Biologics; Quality assurance; Silicone oil; Surfactants; Formulation analysis

Introduction

Ensuring the safety and efficacy of protein-based pharmaceuticals benefits from methods to detect subvisible particulate contaminants, to differentiate them by composition, and to measure the concentrations of each population of particles in dispersion.¹ We previously have demonstrated that holographic video microscopy (HVM) can detect individual contaminant particles ranging in size from 500 nm to 10 μ m and can differentiate subvisible

This is an open access article under the CC BY-NC-ND license (<http://creativecommons.org/licenses/by-nc-nd/4.0/>).

*Corresponding author. laphilips@gmail.com, (L.A. Philips).

Appendix A. Supplementary Data

Supplementary data to this article can be found online at <https://doi.org/10.1016/j.xphs.2020.05.002>.

protein aggregates from silicone oil emulsion droplets on the basis of their differing refractive indexes.^{2,3} Here, we demonstrate that HVM can detect, differentiate and identify multiple distinct populations of subvisible particles when they are present simultaneously in complex heterogeneous dispersions, including the most common categories of subvisible contaminants that are introduced into biopharmaceutical products during the various stages of development, manufacturing and use. These include subvisible protein aggregates in combination with oil droplets,^{4,5} degradants of surfactants,⁶ metal particles⁷ and air bubbles.⁸ All such particle types are indistinguishable to conventional particle characterization technologies including microflow imaging (MFI) and HIAC.⁸ They are rapidly and reliably detected, differentiated and quantitated by HVM.

Differentiating colloidal particles by refractive index is a unique capability of HVM relative to other particle characterization techniques.^{2,9} Single-particle HVM measurements proceed rapidly enough to build up statistics on tens of thousands of particles in 20 min.^{10–13} These results then yield the concentrations and size distributions of each population of particles in a complex mixture.^{2,14}

Real-world biopharmaceutical products not only play host to a wide variety of contaminant particles, but also have widely varying physical characteristics, most notably variations in viscosity that can pose challenges to standard measurement techniques. Previous HVM studies of protein aggregation have been performed in water with a viscosity around 1 cP.^{2,3} We establish through measurements on NIST-traceable colloidal standards that HVM also yields correct results for the diameter and refractive index of subvisible colloidal particles across the commercially relevant range of viscosities, up to 20 cP. Titration studies also show that HVM provides consistent results for concentration across this range.

Changes in medium composition can influence the refractive index of the medium. Medium refractive index, however, does not influence holographic characterization of compact objects such as oil droplets, metal particles, and air bubbles, whose intrinsic light-scattering properties are not influenced by the medium.^{15,16} Changes in the medium's refractive index do change the signature of porous objects such as protein aggregates, whose measured refractive indexes track changes in the index of the medium. Such changes also can be used to distinguish protein aggregates from other, compact homogeneous contaminants.

Some contaminants, such as the fatty-acid breakdown products of standard surfactants, have quite similar optical characteristics to protein aggregates. Their presence nonetheless can be inferred from holographic characterization measurements through their influence on the distribution of detected particle properties.

Methods and Materials

Holographic Video Microscopy

Holographic video microscopy measurements are performed with xSight (Spheryx, Inc.), which is a turn-key commercial implementation of the holographic characterization instrument described in Wang et al.² The measurement principle is presented in Figure 1. Characterizing a sample involves pipetting a 30 μ L aliquot into the reservoir of a disposable

xCell microfluidic sample chip. xSight engages a vacuum pump with the chip to pull the sample in a pressure driven Poiseuille flow through the xCell's observation volume, where it is illuminated by a collimated laser beam at a vacuum wavelength of 447 nm. Colloidal particles in the fluid stream scatter some of this illumination to the focal plane of an optical microscope, where it interferes with the rest of the beam. The microscope magnifies the resulting interference pattern and relays it to a video camera that records its intensity.

Each snapshot recorded by xSight's camera constitutes a hologram of the particles in the xCell's observation volume and therefore encodes information about the particles' three-dimensional positions, their diameters and their refractive indexes. This information is extracted by fitting each single-particle hologram to a generative model¹⁷ based on the Lorenz-Mie theory of light scattering.^{18,19} Details of the analysis are presented in the Appendix.

Each fit yields the particle's diameter, d_p , with a precision of ± 5 nm and its refractive index, n_p , to within ± 0.003 .¹¹ Holographically measured tracking data are used to follow each particle's motion through the sample volume, both to validate the flow profile and also to provide multiple independent measurements of each particle's properties.

Holographic measurements of particle sizes and refractive index are parameterized by the wavelength of light, the magnification of the microscope, and the refractive index, n_m , of the fluid medium, the last of which can be obtained at part-per-thousand precision with an Abbe refractometer. No additional calibration measurements are required. Instrumental precision and accuracy are validated by measurements on NIST standard particles, as described in Wang et al.²

Holographic video microscopy is most effective for subvisible particles ranging in diameter from 500 nm to 10 μ m and for concentrations ranging from 10^3 particles/mL to 10^7 particles/mL.² A 20-min measurement inspects all of the particles in 3 μ L of the sample, yielding estimates for particle concentrations whose precision is limited on the low end by counting statistics and on the high end by occlusion.³

A particle's refractive index is determined by its composition^{12,17} and thus provides a basis for differentiating subvisible contaminants of different composition. HVM is unique among particle characterization techniques in its ability to provide this information.⁹

Preparation of Dispersions of Subvisible Particles

The model multicomponent colloidal dispersions analyzed in this study are created by mixing stock solutions, emulsions and single-component colloidal dispersions in clean 12 mL vials, inverting 10 times and then vortexing for 10 s. Although vortexing can introduce air bubbles in some samples, any such bubbles would not compromise HVM analysis of particle properties because HVM can distinguish air bubbles from other particles. Freshly mixed samples are transferred immediately into the 30 μ L reservoir of a fresh xCell channel for analysis. All raw materials are used as delivered by the supplier.

Immunoglobulin G (IgG) Aggregates

A stock solution of human IgG is prepared by dissolving lyophilized low-endotoxin IgG (Molecular Innovations, catalog no. HU-GF-ED) in filtered DI water at room temperature to a concentration of 16 mg/mL. IgG readily forms subvisible aggregates under these conditions, as is confirmed by HVM measurements.

Polystyrene Standard Spheres

NIST-traceable polystyrene spheres (Bangs Laboratories, catalog no. NT16 N) with a nominal diameter of $d_p = 1.54 \mu\text{m}$ are dispersed in DI water at a concentration of 4×10^6 particles/mL. HVM confirms a population-mean diameter of $d_p = 1.54 \pm 0.05 \mu\text{m}$ and a refractive index of $n_p = 1.603 \pm 0.003$, which is consistent with expectations for polystyrene.

Silica Standard Spheres

NIST-traceable silica spheres (Bangs Laboratories, catalog no. SS04 N) with a nominal diameter of $d_p = 2.2 \mu\text{m}$ are dispersed in DI water at a concentration of 4×10^6 particles/mL. HVM confirms a population-mean diameter of $d_p = 2.20 \pm 0.05 \mu\text{m}$ and a refractive index of $n_p = 1.424 \pm 0.005$, which is consistent with expectations for silica.

Silicone Oil Emulsion

Silicone oil (Sigma-Aldrich catalog no. 378399, CAS no. 63148-62-9, MDL no. MFCD00132673, 1 cP) is added to DI water at 26 mg/mL. The sample is shaken vigorously by hand to disperse the silicone oil as emulsion droplets. HVM confirms that the resulting droplets have a broad distribution of diameters but a narrow distribution of refractive indexes centered at $n_p = 1.410 \pm 0.003$.

Oleic Acid Dispersion

Oleic acid (90%, Sigma-Aldrich catalog no. 364525, CAS no. 112-80-1, MDL no. MFCD00064242) is dissolved in methanol (99%, Sigma-Aldrich catalog no. M3641, CAS no. 67-56-1, MDL number MFCD00004595) at 0.2% by volume and then is precipitated as droplets by 10X dilution in DI water.

Stearic Acid Dispersion

Stearic acid (98%, Alfa Aesar catalog no. A12244, CAS no. 57-11-4) is dissolved in methanol at a concentration of 9 mg/mL. Aggregates of stearic acid particles are precipitated from this solution by $10 \times$ dilution in DI water. This dispersion then is further diluted by a factor of 100 in DI water.

Tungsten Particles

Tungsten particles (US Research Nanomaterials catalog no. US5014) with a nominal diameter of $d_p = 300 \text{ nm}$ are added to DI water at 13.6 mg/mL and are dispersed by vortexing for 15 s.

Air Bubbles

Micrometer-scale air bubbles are introduced directly into the reservoir of an xCell by rapidly ejecting an aqueous solution of polysorbate 20 (PS20) and sucrose from a 31G insulin syringe (Sure Comfort U-100). The solution uses 1 mg/mL PS20 (Alfa Aesar catalog no. L15029, CAS no. 9005–64-5) as a foaming agent and 64 % wt sucrose (Carolina Biological Supply catalog no. 892860, CAS no. 57–50-1, MDL no. MFCD00006626) to increase the viscosity to roughly 20 cP.²¹

Tuning the Dispersion's Refractive Index

The refractive index, n_m , of the aqueous medium is adjusted by adding sucrose (Carolina Biological Supply, catalog no. 892860, CAS no. 57–50-1, MDL no. MFCD00006626) or glycerol (Sigma-Aldrich, catalog no. G5516, CAS no. 56–81-5, MDL no. MFCD00004722). In each case the dispersion to be studied is prepared as a stock sample at 10X the desired particle concentration. The same stock dispersion then is diluted to 10 v/v% for each preparation in an aqueous solution of sucrose or glycerol whose concentration is chosen to provide a desired value of n_m .²² The actual value of n_m is determined with an Abbe refractometer (Edmund Optics). This value also is used to confirm the concentration of sucrose or glycerol in solution.²² Diluting a stock dispersion by a fixed proportion ensures that the same concentration of particles is present in each dispersion across the range of refractive indexes studied.

Sucrose and glycerol both increase the viscosity of aqueous solutions. xSight accommodates samples with viscosities ranging from 1 cP to 25 cP, which encompasses the range of dispersion viscosities used in this study. The precise value of the viscosity is not required for successful HVM measurements and is estimated from the solution's concentration.^{21,23}

Results

Detection and Differentiation of Subvisible Contaminant Particles in a Complex Heterogeneous Sample

Figure 2(a) shows HVM results for a sample containing a mixture of protein aggregates, silicone oil emulsion droplets and droplets of oleic acid. Each of the 18,892 discrete points in the scatter plot represents the diameter, d_p , and refractive index, n_p , of a single particle that was detected in 3 μL of the sample. The dots fall into clusters that represent different populations of particles. The density of measurements, $\rho(d_p, n_p)$, therefore offers insights into the composition of the sample. Each point in Figure 2(a) is colored by the density of particles, $\rho(d_p, n_p)$, as indicated by the color bar.

The size distribution of all of the particles in the sample, $\rho(d_p)$, is presented in Figure 2(b). It combines information from all 3 populations of particles and does not provide a basis for distinguishing among them. This projected size distribution shows that there are many more small particles than large in this sample, down to the 500 nm lower detection limit of the instrument. The decrease in observed particle concentration for the smallest particles reflects the loss of detection sensitivity near the instrumental limit.

The multicomponent nature of the sample is clearly evident in the projected distribution of single-particle refractive indexes, $\rho(n_p)$, which is plotted in Figure 2(c). Broadly speaking, this plot reveals 3 populations of particles, each represented as a distinct peak in $\rho(n_p)$. The nature of each population is revealed in the joint distribution of single-particle sizes and refractive indexes in Figure 2(a). The lowest-index population of particles appears as an extended horizontal stripe in $\rho(d_p, n_p)$, which means that the detected particles have a wide range of sizes, but a narrow distribution of refractive indexes. Such horizontal stripes are characteristic of emulsions whose droplets all have the same composition and therefore have similar refractive indexes.

The low-index population has a refractive index of $n_p = 1.410 \pm 0.003$, which is below that of the medium, as indicated by the horizontal dashed line in Figure 2. The 2 higher-index populations have refractive indexes higher than that of the medium. These results show that HVM works equally well for particle indexes above and below the index of the medium, even when low- and high-index particles appear in the same sample.

Particles in the middle population have a broad range of sizes and refractive indexes very close to that of the medium. Within this population, smaller particles tend to have higher refractive indexes. These trends are characteristic of porous particles whose pores are filled with the medium.^{2,3,24,25} Their measured refractive indexes are intermediate between that of the particle's matrix and that of the medium.^{15,16} HVM has been demonstrated to yield accurate characterization data for such inhomogeneous and aspherical particles^{2,16,24–26} through the effective medium theory of light scattering.^{15,27} In this case, the population of particles near the medium refractive index is naturally identified with protein aggregates, as distinct from emulsion droplets.

The highest-index peak is centered symmetrically around $n_p = 1.475 \pm 0.010$, which is slightly lower than the previously published value of 1.489 for oleic acid at the imaging wavelength.²⁸ Aerosol droplets of oleic acid precipitated from alcohol are reported to remain in fluid state.²⁹ Smaller droplets, however, are found to aggregate into irregular clusters without coalescing.³⁰ This would account for the slightly low value of the measured refractive index and the comparatively broad distribution of refractive index values.^{2,15,24,25}

This interpretation of the HVM data is supported by characterization measurements performed on the component single-population samples independently. These measurements yield the refractive index distributions plotted in Figure 2(d) whose superimposed peaks correspond with those in the mixed sample. Slight differences in the peak shapes may reflect interactions among particles from different populations in the mixed sample.

Inorganic Particles: Air Bubbles and Metal Particles

Air bubbles tend to form in viscous formulations subjected to agitation or fast ejection from syringes.^{31,32} Figure 3(a) shows that HVM can distinguish bubbles from dispersed particles and droplets by their refractive index, $n_p = 1.00$, which is the refractive index for most gases, including air. This natural basis for identifying bubbles is an advantage of HVM relative to techniques such as HIAC and FlowCAM that cannot easily differentiate subvisible bubbles from other suspended and dispersed species.^{33,34}

Metal fragments similarly have a clear HVM signature, as can be seen in the data for tungsten particles presented in Figure 3(b). Metal particles tend to have refractive indexes that are substantially higher than organic matter. Tungsten and other metal particles can contaminate pharmaceutical products at all stages of manufacturing and can influence product stability, efficacy and safety.³⁵ Metal particles also are not readily distinguished from other dispersed species by standard particle characterization techniques.^{33,34} The particles reported in Figure 3(b) have a mean refractive index of $n_p = 1.85 \pm 0.09$ which greatly exceeds values for protein aggregates, silicone oil, or degradants such as breakdown products of surfactants. Refractive index therefore provides a natural basis for identifying metal particles in multicomponent dispersions.

Differentiating Subvisible Spheres: Air Bubbles and Silicone Oil Droplets

Being perfectly spherical, air bubbles and silicone oil droplets are readily differentiated from irregular aggregates with conventional imaging techniques, but can be challenging to distinguish from each other. The data in Figure 4 demonstrate that HVM unambiguously differentiates air bubbles from silicone oil droplets on the basis of refractive index when both appear in the same sample. The refractive index of silicone oil droplets depends on the chemical composition of the oil. Air bubbles all have the same refractive index, $n_p = 1.000$.

The peak placement in the measured distribution, $\rho(n_p)$, further validates the precision and accuracy of HVM for single-particle measurement. The refractive index of each detected particle is discovered by fitting rather than being assumed *a priori*. The peak associated with the air bubbles therefore, provides an unambiguous reference point.

Concentration Measurements

In addition to detecting and differentiating different types of particles in a multicomponent sample, HVM also accurately measures the concentration of each of the populations. We demonstrate this capability with a series of samples composed of an aqueous dispersion of 1.5 μm -diameter polystyrene spheres and 2.2 μm -diameter silica spheres diluted to an overall concentration of 1.5×10^6 particles/mL by the addition of glycerol/water solutions. Depending on the final concentration of glycerol, the medium's refractive index ranges from $n_m = 1.34$ for pure water to $n_m = 1.44$. Over the same range, the medium's viscosity ranges from 0.89 cP to nearly 20 cP. The particles' diameters and refractive indexes, however, should remain constant throughout, as should the concentrations of the 2 populations.

HVM readily distinguishes the 2 population of spheres both by diameter and also by refractive index, as can be appreciated from Figure 5(a) and (b). Results for d_p and n_p , moreover, are independent of the medium's refractive index and viscosity, as expected.

Dividing the number of particles detected in each population by the volume of fluid analyzed yields that population's concentration. Figure 5(c) shows the detected concentrations of the 2 populations of spheres over the same range of medium compositions. These concentrations also are independent of the medium's composition, except for a very narrow range of refractive-index values centered around $n_m = 1.422$. In this window, the silica spheres are index-matched to the medium, and so cannot be detected and counted by optical means. This effect does not influence the measured concentration of polystyrene

spheres codispersed in the same medium because polystyrene's refractive index, $n_p = 1.601$, differs substantially from that of the medium.

Index matching affects concentration measurements over a remarkably narrow range of refractive indexes. The solid curve in Figure 5(c) is a Gaussian with width $n_p = 0.002$. HVM reliably detects and reports the concentration of particles whose refractive indexes differ by more than n_p from n_m . The reported concentration values, moreover, do not depend on the physical properties of the medium, including chemical composition, viscosity and refractive index.

Influence of the Medium

Changes in the properties of the medium due to added excipients can influence the results of HVM measurements, most notably for porous particles whose pores are perfused with the medium.^{15,16} The effective refractive index reported by HVM for such particles is intermediate between the refractive index of the medium and the refractive index of the porous particles' matrix material. This mechanism was invoked in the discussion of protein aggregates' properties presented in Figure 2. The data in Figure 6 show this mechanism in action. These results are obtained for mixtures of IgG aggregates and polystyrene spheres in solutions with 0%, 30% and 60% sucrose by weight. These solutions have refractive indexes of $n_m = 1.335$, 1.377 and 1.438, respectively, and viscosities of 1 cP, 3 cP and 58 cP, respectively.

The polystyrene particles in these dispersions yield refractive indexes consistent with $n_p = 1.610 \pm 0.005$, independent of medium composition and in agreement with the results from Figure 5(b). Polystyrene spheres are non-porous and hydrophobic, which means that the medium should not influence their optical properties, as observed.

The mean refractive index of protein aggregates tracks the refractive index of the medium. The distribution of refractive index values furthermore narrows as the refractive index of the medium increases toward the refractive index of protein. Both of these trends are consistent with predictions of the Maxwell Garnett effective medium theory for light-scattering by inhomogeneous media.^{15,16,24,25,27}

Influence of Handling

Handling conditions can change the concentration and composition of the particles in a protein solution. The data in Figure 7(a) show the refractive index distribution, $\rho(n_p)$, for a solution of human IgG in water ($n_m = 1.340$) as a function of ejection rate from a 1 mL syringe through a 31G needle. The syringes used for this study (Beckton-Dickinson, BD Safety-Glide™ 1 mL insulin syringe with BD Ultra-Fine™ needle) are lubricated with silicone oil and are known to release oil droplets.³⁶

The distribution shows 2 populations of particles, one peaked asymmetrically around $n_p = 1.36$ and the other centered symmetrically and more narrowly around $n_p = 1.41$. We interpret the former as representing a population of protein aggregates, and the latter as arising from a population of silicone oil droplets.

The concentration and distribution of particle properties clearly changes as the ejection rate is increased from 10 $\mu\text{L/s}$ up to 120 $\mu\text{L/s}$. To quantify these trends, we fit $\rho(n_p)$ to the sum of a symmetric Gaussian distribution representing the silicone oil droplets and an asymmetric Gamma distribution representing protein aggregates. These fits appear as shaded regions in Figure 7(a), with lighter (yellow) shading corresponding to the fit for protein aggregates and darker (cyan) shading corresponding to silicone oil droplets.

The areas under these curves correspond to the numbers of particles of each type observed in 0.5 μL of the sample. The associated concentrations are plotted as a function of ejection rate in Figure 7(b). Essentially no silicone oil droplets appear in the sample ejected at low flow rates. Faster flows elute more silicone oil droplets, with the concentration rising to 2000 droplets/mL at an ejection rate of 120 $\mu\text{L/s}$. Interestingly, the concentration of protein aggregates doubles over the same range of ejection rates. This trend is only visible because HVM differentiates the 2 types of particles. The data in Figure 7 therefore highlight the value of HVM for detecting and interpreting changes in protein solutions induced by handling, in this case flow-induced changes.

Figure 8 shows the distribution of particle diameters, $\rho(d_p)$ for the same samples, presented as a function of ejection rate. For each sample, curves show the total distribution for all particles in the sample as well as separate distributions for the IgG aggregates and silicone oil droplets that were differentiated by refractive index. Consistent with the conclusions drawn from the refractive-index data in Figure 7, increased elution rate increases the concentration of aggregates and oil droplets alike at all sizes.

Discussion

Holographic video microscopy detects the wide variety of subvisible particle types that can be present in biologic pharmaceutical formulations and provides a physical basis for differentiating the different species, quantifying their properties and measuring their concentrations. The data presented here demonstrate that HVM yields accurate results for NIST-traceable particle standards, subvisible protein aggregates, silicone oil emulsion droplets, air bubbles, metal particles and fatty acids that model the breakdown products of common surfactants. HVM provides consistent results, furthermore, in fluid media whose viscosities range from 1 cP to at least 20 cP.

In cases such as the model system in Figure 2, disparate populations of particles can coexist in a multicomponent dispersion without influencing each other's properties. The results from this kind of heterogeneous mixture is apparent from the HVM data in Figure 2(c) and (d) because the distribution of properties in a three-component sample can be reconstituted as a superposition of the 3 separate stock samples.

In other cases, the particles in a heterogeneous dispersion interact, yielding measurable changes in the sample's HVM signature. The data in Figure 9 illustrate such a change. These data were acquired for IgG aggregates, stearic acid particles, and a mixture of these 2 types of particles, each dispersed in water. Figure 9(a) presents the distribution of particle diameters, $\rho(d_p)$, for each of these 3 samples together with the difference, $\rho(d_p)$, between

the size distribution of the mixture and the combined size distribution for the 2 homogeneous components. Figure 9(b) shows the corresponding results for the distribution of refractive indexes, $\rho(n_p)$ and $\rho(n_p)$.

Stearic acid particles are not readily differentiated from protein aggregates either by size or by refractive index because the 2 populations of particles have similar optical properties. The mixed sample, however, has distinctly different properties from either of the components. The presence of stearic acid in a dispersion of IgG aggregates shifts the size distribution toward smaller particles than were in either parent population and simultaneously shifts the refractive index distribution to higher values. The observed transformation of the HVM signature suggests that stearic acid may promote restructuring of branched protein aggregates into denser, more compact forms. No such transformation is evident in Figure 2 when droplets of silicone and oleic acid are added to a dispersion of IgG aggregates. This distinction suggests that stearic acid may interact with protein aggregates in a different manner than other codispersed species, and thus highlights the differing influences that may be exerted by breakdown products of different surfactants used in biopharmaceuticals.

These complementary and contrasting examples demonstrate the new window that HVM provides into the microstructure and composition of subvisible particles. The ability to detect particles with widely varying physical properties, to distinguish them by size and composition and to measure their concentrations provides valuable information that can be used to diagnose problems in formulation, manufacturing, distribution and storage of biopharmaceutical products.

Supplementary Material

Refer to Web version on PubMed Central for supplementary material.

Acknowledgments

Research reported in this publication was supported by the National Center For Advancing Translational Sciences of the National Institutes of Health under Award Number R44TR001590. The content is solely the responsibility of the authors and does not necessarily represent the official views of the National Institutes of Health.

References

1. Ratanji KD, Derrick JP, Dearman RJ, Kimber I. Immunogenicity of therapeutic proteins: influence of aggregation. *J. Immunotoxicol.* 2014;11:99–109. [PubMed: 23919460]
2. Wang C, Zhong X, Ruffner DB, et al. Holographic characterization of protein aggregates. *J Pharm Sci.* 2016;105:1074–1085. [PubMed: 26886303]
3. Kasimbeg PN, Cheong FC, Ruffner DB, Blusewicz JM, Philips LA. Holographic characterization of protein aggregates in the presence of silicone oil and surfactants. *J Pharm Sci.* 2019;108:155–161. [PubMed: 30315809]
4. Felsovalyi F, Janvier S, Jouffray S, Soukiassian H, Mangiagalli P. Silicone-oil-based subvisible particles: their detection, interactions, and regulation in prefilled container closure systems for biopharmaceuticals. *J Pharm Sci.* 2012;101:4569–4583. [PubMed: 23023774]
5. Shah M, Rattray Z, Day K, et al. Evaluation of aggregate and silicone-oil counts in pre-filled siliconized syringes: an orthogonal study characterising the entire subvisible size range. *Int J Pharm.* 2017;519:58–66. [PubMed: 28089934]

6. Martos A, Koch W, Jiskoot W, et al. Trends on analytical characterization of polysorbates and their degradation products in biopharmaceutical formulations. *J Pharm Sci.* 2017;106:1722–1735. [PubMed: 28302541]
7. Anil KT, Randolph TW, Dong A, Maloney KM, Hitscherich C Jr, Carpenter JF. Igg particle formation during filling pump operation: a case study of heterogeneous nucleation on stainless steel nanoparticles. *J Pharm Sci.* 2009;98:94–104. [PubMed: 18454482]
8. Scherer TM, Leung S, Owyang L, Shire SJ. Issues and challenges of subvisible and submicron particulate analysis in protein solutions. *AAPS J.* 2012;14:236–243. [PubMed: 22391789]
9. Xu R. Particle Characterization: Light Scattering Methods, Particle Technology Series. Dordrecht: Kluwer Academic Publishers; 2001.
10. Cheong FC, Sun B, Dreyfus R, et al. Flow visualization and flow cytometry with holographic video microscopy. *Opt Express.* 2009;17:13071–13079. [PubMed: 19654712]
11. Krishnatreya BJ, Colen-Landy A, Hasebe P, et al. Measuring Boltzmann's constant through holographic video microscopy of a single sphere. *Am J Phys.* 2014;82:23–31.
12. Yevick A, Hannel M, Grier DG. Machine-learning approach to holographic particle characterization. *Opt Express.* 2014;22:26884–26890. [PubMed: 25401836]
13. Hannel MD, Abdulali A, O'Brien M, Grier DG. Machine-learning techniques for fast and accurate feature localization in holograms of colloidal particles. *Opt Express.* 2018;26:15221–15231. [PubMed: 30114772]
14. Philips LA, Ruffner DB, Cheong FC, et al. Holographic characterization of contaminants in water: differentiation of suspended particles in heterogeneous dispersions. *Water Res.* 2017;122:431–439. [PubMed: 28624726]
15. Cheong FC, Xiao K, Pine DJ, Grier DG. "Holographic characterization of individual colloidal spheres' porosities. *Soft Matter.* 2011;7:6816–6819.
16. Odete MA, Cheong FC, Winters A, Elliott JJ, Philips LA, Grier DG. The role of the medium in the effective-sphere interpretation of holographic particle characterization data. *Soft Matter.* 2020;16:891–898. [PubMed: 31840154]
17. Lee SH, Roichman Y, Yi GR, et al. Characterizing and tracking single colloidal particles with video holographic microscopy. *Opt Express.* 2007;15:18275–18282. [PubMed: 19551125]
18. Bohren CF, Huffman DR. Absorption and Scattering of Light by Small Particles. New York: Wiley Interscience; 1983.
19. Mishchenko MI, Travis LD, Lacis AA. Scattering, Absorption and Emission of Light by Small Particles. Cambridge: Cambridge University Press; 2001.
20. Sultanova N, Kasarova S, Nikolov I. Dispersion properties of optical polymers. *Acta Phys Polonica A.* 2009;116:585.
21. Telis VRN, Telis-Romero J, Mazzotti HB, Gabas AL. Viscosity of aqueous carbohydrate solutions at different temperatures and concentrations. *Int J Food Prop.* 2007;10:185–195.
22. Joao Carlos RR, Lampreia IM, Santos ÂF, Moita ML, Douh ret G. Refractive index of liquid mixtures: theory and experiment. *ChemPhysChem.* 2010;11:3722–3733. [PubMed: 20957714]
23. Segur JB, Oberstar HE. Viscosity of glycerol and its aqueous solutions. *Ind Eng Chem.* 1951;43:2117–2120.
24. Wang C, Cheong FC, Ruffner DB, Zhong X, Ward MD, Grier DG. Holographic characterization of colloidal fractal aggregates. *Soft Matter.* 2016;12:8774–8780. [PubMed: 27722566]
25. Fung J, Hoang S. Assessing the Use of Digital Holographic Microscopy to Measure the Fractal Dimension of Colloidal Aggregates. In: *Novel Techniques in Microscopy.* Optical Society of America; 2019 JT4A.19.
26. Hannel M, Middleton C, Grier DG. Holographic characterization of imperfect colloidal spheres. *Appl Phys Lett.* 2015;107:141905.
27. Markel V. Introduction to the Maxwell Garnett approximation: tutorial. *J Opt Soc Am A.* 2016;33:1244–1256.
28. Yanina IY, Lazareva EN, Tuchin VV. Refractive index of adipose tissue and lipid droplet measured in wide spectral and temperature ranges. *Appl Optic.* 2018;57:4839–4848.

29. Secker DR, Kaye PH, Greenaway RS, Hirst E, Bartley DL, Videen G. Light scattering from deformed droplets and droplets with inclusions. I. Experimental results. *Appl Optic*. 2000;39:5023–5030.
30. Katrib Y, Biskos G, Buseck PR, et al. Ozonolysis of mixed oleic-acid/stearic-acid particles: reaction kinetics and chemical morphology. *J Phys Chem*. 2005;109: 10910–10919.
31. Vincent C, Narhi LO, Spitznagel TM, et al. Subvisible (2–100 µm) particle analysis during biotherapeutic drug product development: Part 2, experience with the application of subvisible particle analysis. *Biologicals*. 2015;43:457–473. [PubMed: 26324466]
32. Randolph TW, Schiltz E, Sederstrom D, et al. Do not drop: mechanical shock in vials causes cavitation, protein aggregation, and particle formation. *J Pharm Sci*. 2015;104:602–611. [PubMed: 25418950]
33. Tobias W, Volkin DB, Mahler HC. Effect of solution properties on the counting and sizing of subvisible particle standards as measured by light obscuration and digital imaging methods. *Eur J Pharm Sci*. 2014;53:95–108. [PubMed: 24370624]
34. Hawe A, Zöls S, Freitag A, Carpenter JF. Subvisible and visible particle analysis in biopharmaceutical research and development In: *Biophysical Characterization of Proteins in Developing Biopharmaceuticals*. Elsevier; 2015:261–286.
35. Miranda MC, Gilli F, Schellekens H, Randolph TW, Jiskoot W. Immunogenicity of recombinant human interferon beta interacting with particles of glass, metal, and polystyrene. *J Pharm Sci*. 2012;101:187–199. [PubMed: 21918983]
36. Melo GB, Junior CD, Carvalho MR, et al. Ana carolina miglorini figueira, acácio alves souza Lima filho, geoffrey guy emerson, and maurício maia, “release of silicone oil droplets from syringes. *Int J Retina Vitreous*. 2019;5:1. [PubMed: 30788149]

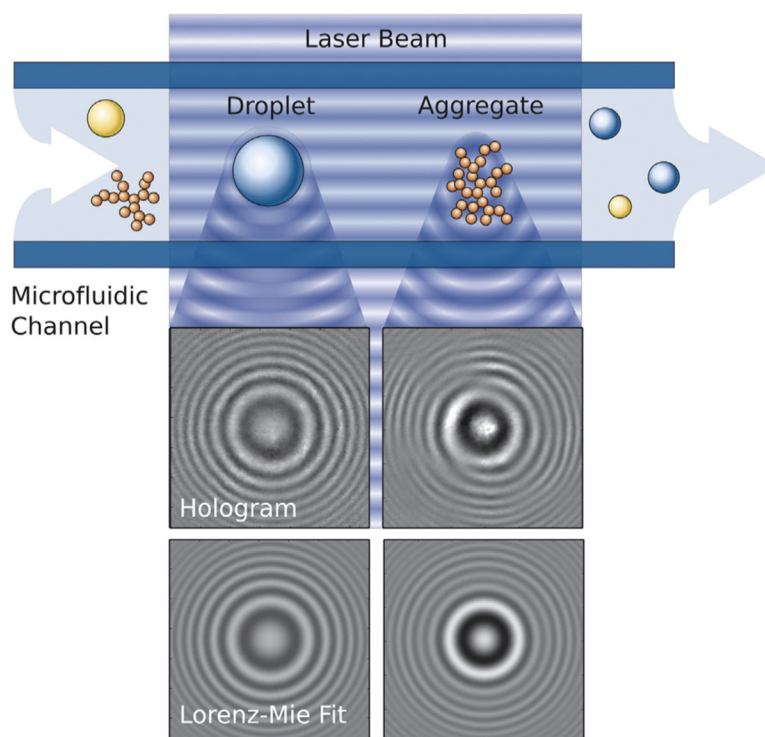


Figure 1. Principle of holographic particle characterization. Subvisible particles flow down a microfluidic channel through a collimated laser beam. Light scattered by a particle interferes with the remainder of the beam to create a hologram of the particle that is magnified by a microscope (not shown) and recorded with a video camera. Each hologram is fit pixel-by-pixel to a generative model derived from the Lorenz-Mie theory of light scattering to obtain that particle's effective diameter and refractive index.

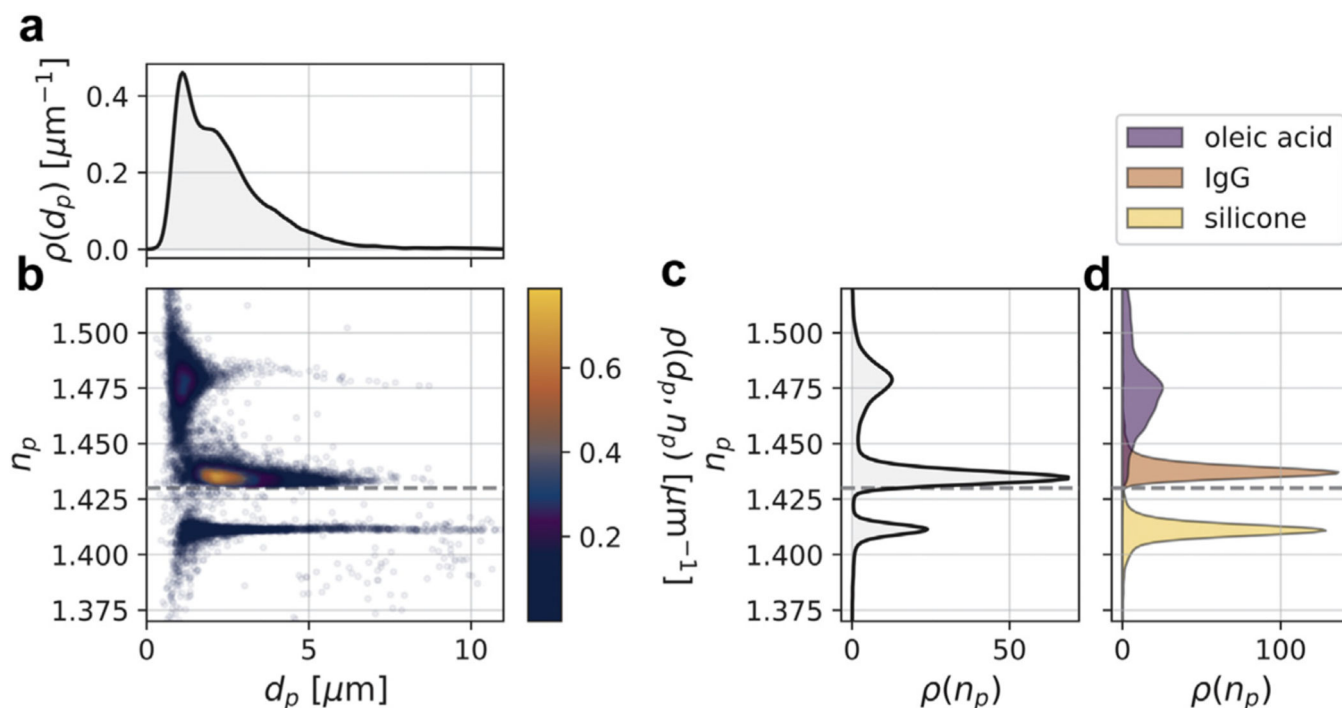


Figure 2.

Holographic characterization of contaminant particles in a solution of human IgG. Suspended particles include IgG aggregates, silicone oil droplets and oleic acid droplets. The aqueous medium includes dissolved sucrose that raises the medium's refractive index to $nm = 1.430 \pm 0.001$ and increases the medium's viscosity. (a) Scatter plot in which each point represents the diameter, d_p , and refractive index, n_p , of one detected particle and is colored by the density of measurements, $\rho(d_p, n_p)$. (b) The projected size distribution, $\rho(d_p)$, yields the total concentration of detected subvisible particles. (c) The projected distribution of refractive indexes, $\rho(n_p)$, distinguishes particles by composition. (d) Superimposed projected refractive index distributions of 3 control samples of oleic acid droplets, IgG aggregates and silicone oil droplets.

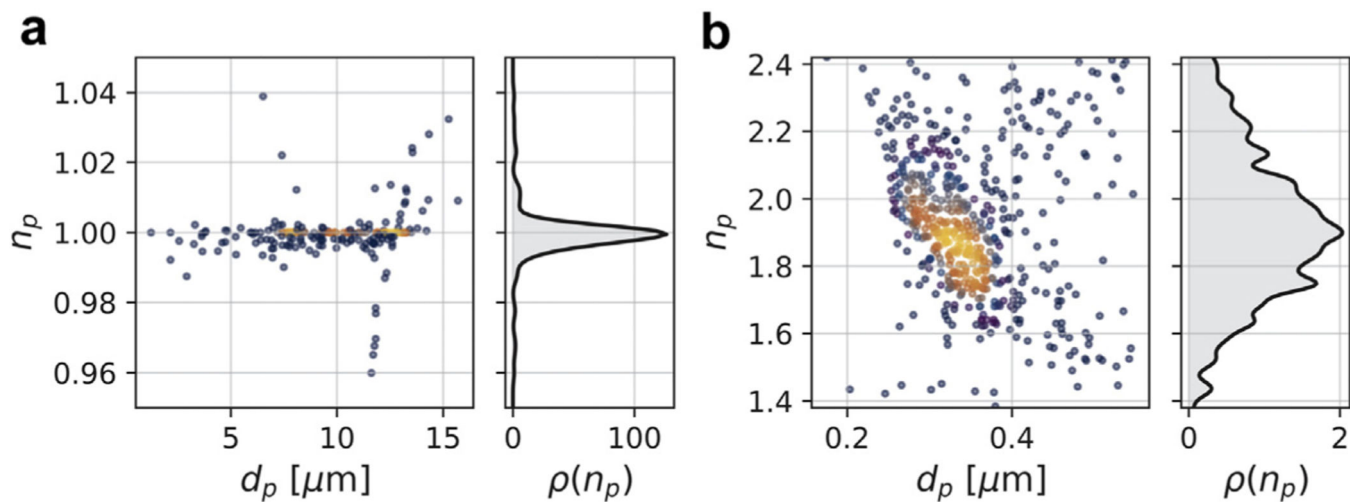


Figure 3. Joint distribution of the diameter, d_p , and refractive index, n_p , of (a) air bubbles and (b) tungsten spheres, together with the projected distributions of refractive indexes, $\rho(n_p)$. Air bubbles have refractive indexes very tightly clustered around $n_p = 1.0$. Monodisperse tungsten spheres display a comparatively small range of diameters, and very high refractive index values.

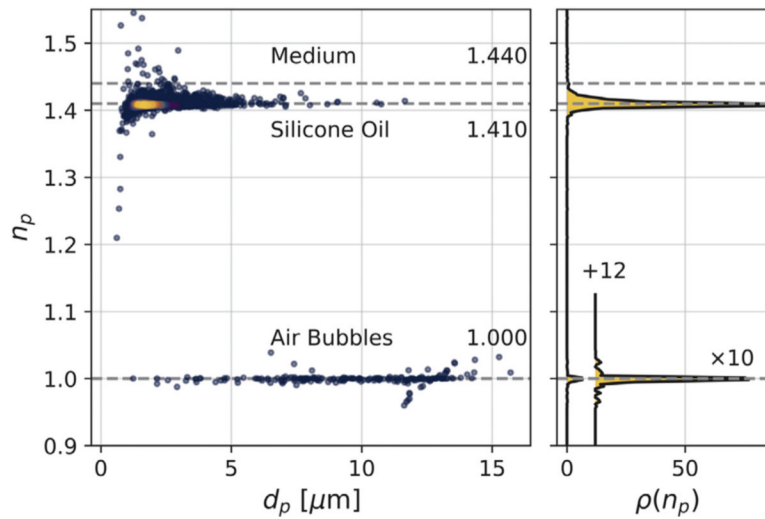


Figure 4. Holographic analysis of silicone oil droplets and air bubbles dispersed simultaneously in a viscous medium. Air bubbles have a refractive index of 1.000. Silicone oil droplets have a refractive index of 1.410. The aqueous medium has a refractive index of $n_m = 1.440$. The distribution of refractive index values, $\rho(n_p)$, shows 2 clearly resolved peaks. There being far fewer bubbles than droplets in this sample, the peak around $n_p = 1.000$ is multiplied by 10 and displaced by 12 for clarity.

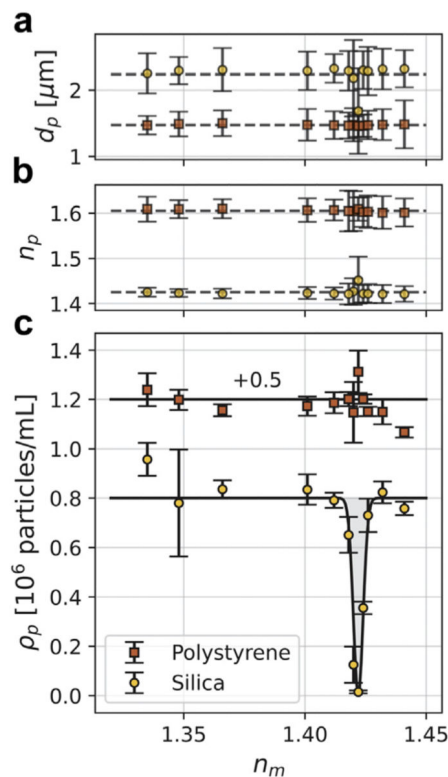


Figure 5.

(a) Population-averaged values for the diameters, d_p , of polystyrene spheres (orange squares) and silica spheres (yellow circles) dispersed in water-glycerol mixtures of varying refractive index, n_m . Measured diameters are independent of n_m . (b) The particles' refractive indexes, n_p , similarly are independent of n_m . (c) Measured concentrations, ρ_p , of polystyrene and silica spheres as a function of n_m . The concentration of each population of particles is reported consistently and is independent of n_m except for a region, $n_p = n_m \pm 0.002$ in which silica spheres are index-matched to the medium and therefore are not detectable. Concentration data for polystyrene spheres are offset upward by 5×10^5 particles/mL for clarity.

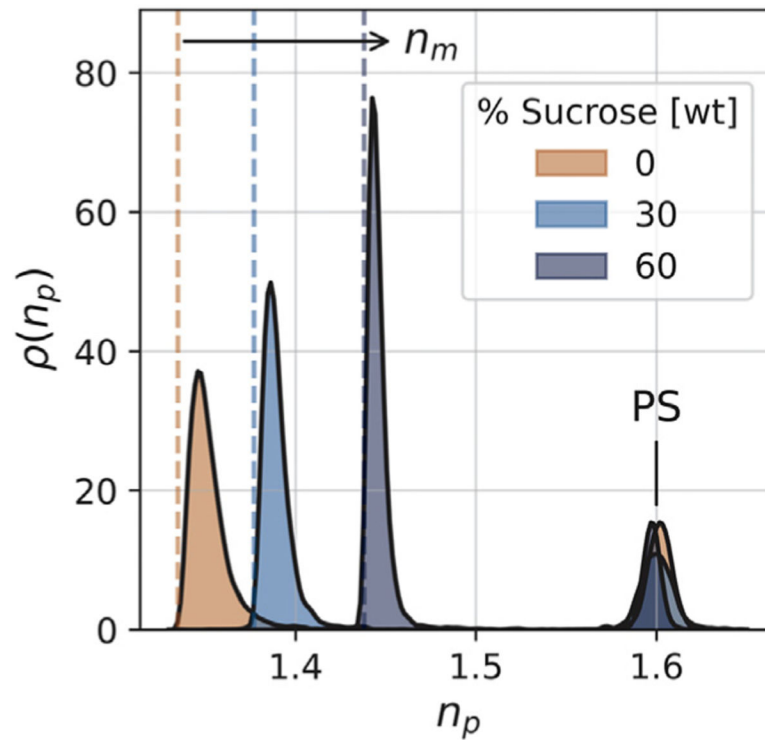


Figure 6. Influence of added sucrose on the holographically measured refractive index distribution of IgG aggregates. Codispersed polystyrene beads (PS) serve as a reference.

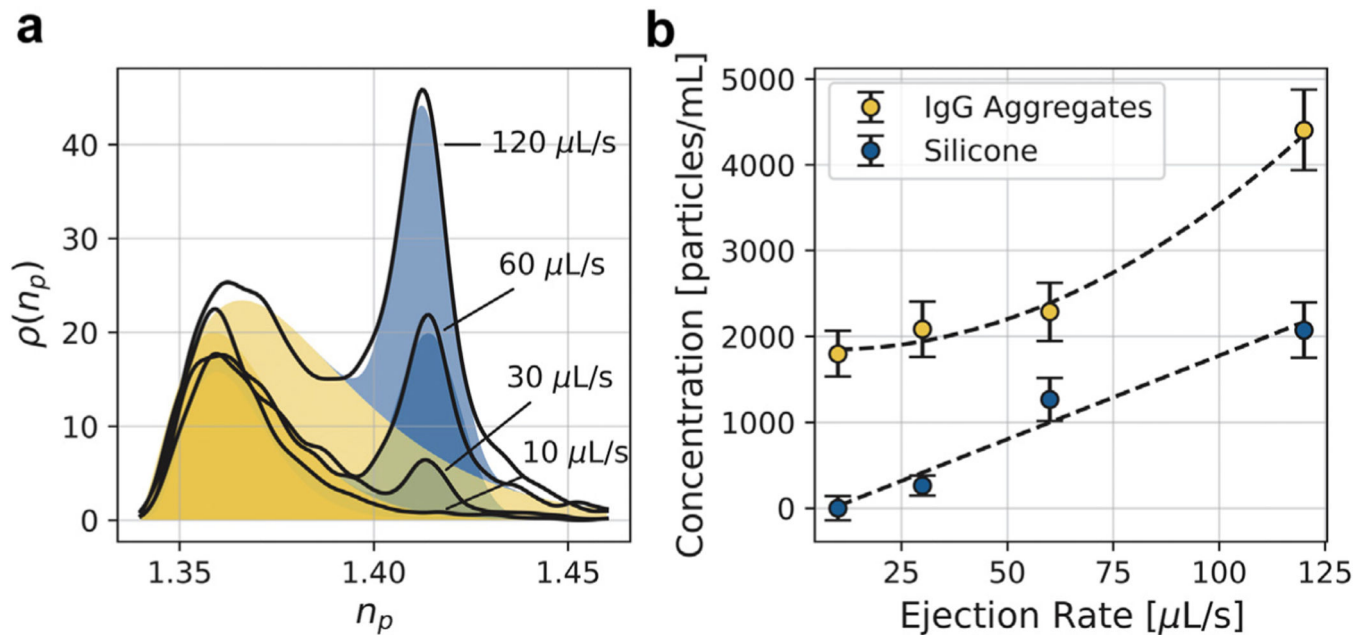


Figure 7.

Influence of syringe ejection rate on particle concentrations. (a) Measured particle refractive index distributions, $\rho(n_p)$, for 4 different ejection rates. Dark (cyan) shaded regions represent the symmetric Gaussian distribution expected for silicone oil droplets. Lighter (yellow) shaded regions represent an asymmetric Gamma distribution for protein aggregates. Their sum is a model for the total measured distribution and serve to identify each population in the sample. (b) Integrated concentrations of protein aggregates and silicone oil emulsion droplets obtained from the data in (a) as a function of ejection rate.

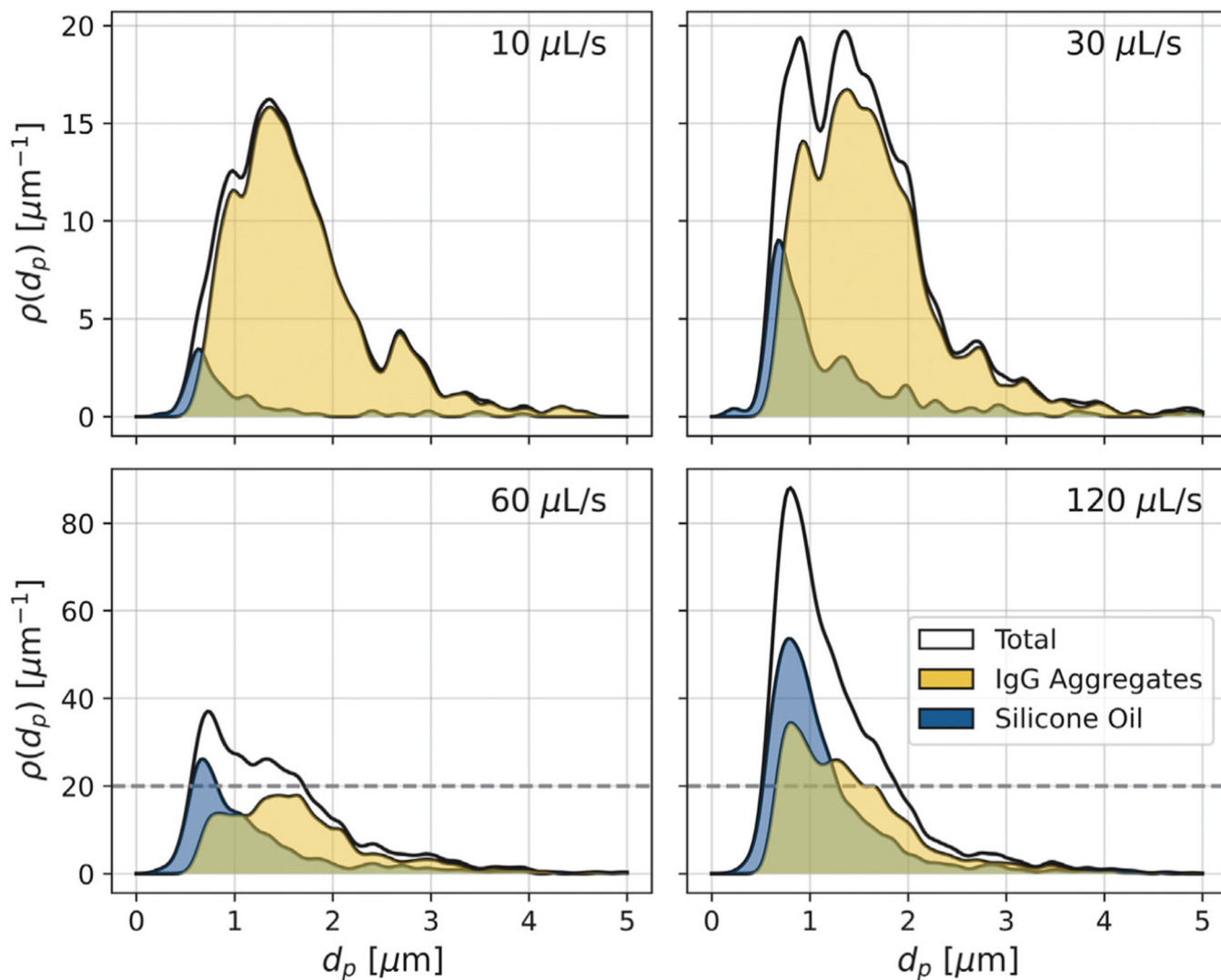


Figure 8. Influence of syringe ejection rate on the distribution of particle diameters, $\rho(d_p)$, in the samples presented in Figure 7. Curves show the total distribution of all detected particles as well as distributions for IgG aggregates and silicone oil emulsion droplets identified on the basis of refractive index.

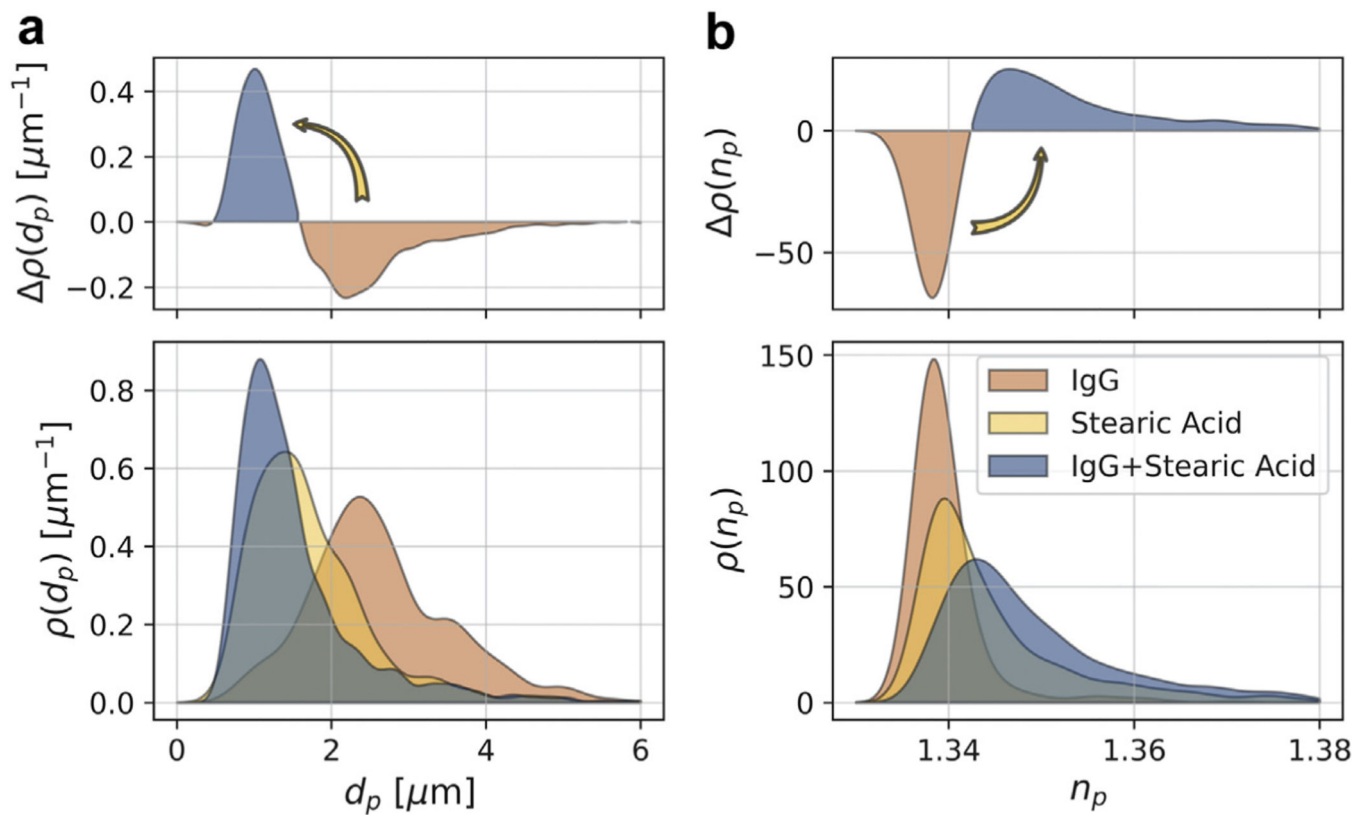


Figure 9.

Interaction between stearic acid and IgG aggregates. (a) Mixing a dispersion of stearic acid particles with a dispersion of IgG aggregates shifts the distribution of particle diameters, $\rho(d_p)$, to smaller sizes. This shift is apparent in the difference, $\rho(d_p)$, between the diameter distribution in the mixed sample and the diameters of stearic acid particles in IgG aggregates individually. (b) The distribution of refractive indexes shifts upward upon mixing. Taken together, (a) and (b) show that the mixture of stearic acid and IgG favors aggregates that are smaller and denser than either IgG or stearic acid alone.